

Simulation Study of the Effects of Polymer Network Dynamics and Mesh Confinement on the Diffusion and Structural Relaxation of Molecular Penetrants

Tsai-Wei Lin^{1,3}, Baicheng Mei^{2,3}, Kenneth S. Schweizer^{1,2,3}, and Charles E. Sing^{1,3}

¹Department of Chemical and Biomolecular Engineering, University of Illinois at Urbana-Champaign

²Department of Materials Science and Engineering, University of Illinois at Urbana-Champaign

³Materials Research Laboratory, University of Illinois at Urbana-Champaign

Abstract

The diffusion of small molecular penetrants through polymeric materials represents an important fundamental problem, relevant to the design of materials for applications such as coatings and membranes. Polymer networks hold promise in these applications, because dramatic differences in molecular diffusion can result from subtle changes in the network structure. In this paper, we use molecular simulation to understand the role that crosslinked network polymers have in governing the molecular motion of penetrants. By considering the local, activated alpha relaxation time of the penetrant and its long-time diffusive dynamics, we can determine the relative importance of glassy dynamics versus mesh confinement on penetrant diffusion. We vary several parameters, such as the crosslinking density, temperature, and penetrant size, to show that crosslinks primarily affect molecular diffusion through modification of the matrix glass transition, with local penetrant hopping at least partially coupled to the segmental relaxation of the polymer network. This coupling is very sensitive to the local glassy dynamics of the surrounding matrix, and we also show that penetrant transport is affected by dynamic heterogeneity at low temperatures. To contrast, only at high temperatures and large penetrants does the effect of mesh

confinement become significant, even though penetrant diffusion empirically follows similar trends as established models of mesh confinement-based transport.

Introduction

The diffusive transport of molecular species through polymers is an important fundamental problem, with the motion of small ‘penetrants’ being integral to the design of polymer materials for a variety of applications. For example, barrier coatings,¹⁻³ drug delivery vehicles,^{4,5} and self-healing microcapsules^{1,2,6} may be engineered to impede the transport of penetrants, while membranes are often designed to selectively separate or filter specific small penetrants (e.g. gas,⁷⁻¹⁰ water,¹¹⁻¹³ or organic molecules^{14,15}). Membrane separations represent an especially important materials design challenge,^{7,15} due to significant interest in finding promising alternatives to distillation for chemical separations. Distillation is a costly and inefficient process that is the source of an estimated 10-15% of the world’s energy consumption,¹⁵ prompting a search for materials that can selectively transport small molecules based on their physicochemical features (e.g. size, shape, or interactions).

The predominant strategy for separating molecules is to impose control over pore size in materials such as zeolites,¹⁶ metal organic frameworks,^{17,18} and covalent organic frameworks.¹⁹ While these form precise structures that are selective to molecular size and chemistry, they are typically very brittle and difficult to synthesize at scale.¹⁶⁻¹⁹ If the molecular penetrants are especially small, such as in gas separations, then glassy amorphous polymers can be another option for membranes.⁸⁻¹⁰ These materials are more mechanically robust, but are limited to small gas molecules and do not have the same size-selectivity as more precise matrix structures. Alternatively, rubbery polymer membranes can instead be tailored to use solubility to affect penetrant transport while retaining high rates of transport even for larger molecules,¹⁴ though this

again suffers from limited selectivity. Despite this abundance of promising strategies for designing separation membranes, the design principles for selectivity relies on a still-incomplete understanding how chemical structure and dynamics contributes to the diffusive transport of molecular penetrants. Highly-crosslinked networks have recently emerged as a promising option for the selective transport of small molecules,^{20–22} exploiting the sensitivity of penetrant diffusion to the near- T_g coupling between the structural relaxation of the dense molecular mesh and activated hopping processes. This is motivated by experimental support for the premise that, despite significant molecular disorder, dense polymer networks can discern small changes in penetrant size and interactions.²¹

Design of crosslinked networks for selective transport requires an understanding of how the molecular-scale dynamics of penetrant and matrix relaxation contribute to large-scale diffusive motion. Aspects of this problem have been studied in the literature. For example, there has been extensive work on studying particle transport through polymer solutions or high-temperature networks,^{23–29} which is understood to be governed by a confinement parameter $C = d/a_x$ that relates the penetrant size d to the size of the network mesh a_x . This parameter quantifies the extent to which the surrounding polymer matrix sterically ‘traps’ the particle, such that the particle diffusion is an activated process where the network strands must entropically stretch to allow the particle to hop out of its location within the mesh.²³ Several expressions for the diffusion constant have been considered in this literature, such as the expression proposed by Cai, et al.:²³

$$D_p \sim \frac{d^2}{\tau} C^{-1} \exp(-bC^2) = \frac{d^2}{\tau} X \quad (1)$$

This relates the diffusion constant D_p to the confinement parameter C , a length scale characterized by the penetrant size d , a time scale τ that Cai, *et al.* identify as the Rouse time of the network strand, and a constant b of order unity.²³ While there are other candidate models,²⁶ these still

exhibit a general form given in the second equivalence of **Equation 1** as the product of two factors; the elementary particle diffusion d^2/τ and a factor X dictated by the network mesh and related to C (in the case above, $X = \exp(-bC^2)/C$). Simulations of large penetrants in rubbery (i.e. high-temperature) networks are consistent with this physical picture;^{24,25,30} however, the choice of τ can become non-trivial as temperature is lowered for polymer melts and/or when the glass transition is approached.³¹ For example, in uncrosslinked systems activated transport of penetrants and particles becomes dominated by molecular caging near the glass transition.³¹⁻³⁴

For tight and near- T_g networks, the physical relationship in **Equation 1** is complicated by recent experimental, simulation, and theoretical investigations by the authors and collaborators demonstrating that the structural relaxation in polymer networks is strongly dependent on the extent of crosslinking, manifesting as a monotonic increase in the material T_g with crosslink density.³⁵ In this case, the time scale τ in **Equation 1** is expected to depend on molecular penetrant caging, which itself will be sensitive to the confinement parameter C due to its relationship with the crosslink density of the polymer network. Crosslinks could thus impact penetrant motion both by affecting the structural relaxation of the surrounding network as well as providing a confining mesh that obstructs penetrant motion.

In this article, we use computer simulation to study the diffusion of penetrants in dense, highly-crosslinked polymer networks in the weakly-supercooled regime. Simulation will allow us to separate out the different ways that crosslinks contribute to penetrant diffusion, by quantifying both the overall diffusion constant D_p and the characteristic time scale of penetrant hopping $\tau = \tau_{\alpha,p}$ that we identify with a penetrant alpha relaxation time. By relating particle hopping events to long-time diffusive motion, we can study how these properties are affected by both crosslinking fraction and temperature. We determine that (1) supercooled networks exhibit strong coupling

between the network segmental relaxation and penetrant hopping, with sensitivity to the crosslinking-dependent T_g , (2) increasing temperatures can lead to slower diffusion at a given T_g/T due to the dependence of T_g on crosslink density, but this is mostly attributed to a non-trivial T dependence of how local polymer relaxations couple to penetrant motion, (3) the coupling between penetrant motion and polymer relaxation processes is dependent on penetrant size d , and (4) molecular penetrant hopping is correlated with long-time diffusion at several values of T_g/T near $T = T_g$, but the mesh confinement only becomes apparent at high T and for large penetrants. This all leads to the overall insight that, under typical conditions for polymer networks and molecular penetrants, crosslinking primarily affects penetrant transport by changing the effective T_g of the surrounding matrix and only *secondarily* through mesh confinement. Serendipitously, this still manifests in a similar relationship between the diffusion constant D_p and C that is consistent with the form in **Equation 1**.^{23,26} These molecular-level insights into penetrant diffusion and hopping clarify the fundamental mechanisms governing penetrant transport and help identify ways in which both temperature and network architecture can be used to engineer selectivity into a promising class of membrane materials.

Simulation Methods

We use coarse-grained molecular dynamics simulations (MD) to model the diffusion of spherical penetrants in crosslinked polymer networks,³⁶ using well-established methods for studying polymers near the glass transition.³⁷⁻⁴⁰ Our system is initially composed of $N_c = 20$ linear chains with $N_m = 30$ beads each with diameter σ , modeled as standard semiflexible chains. These beads are placed in a cubic box with periodic boundary conditions in three dimensions, along with N_p spherical penetrants of diameter \tilde{d} . The number of penetrants N_p depends on \tilde{d} , and is chosen so that the volume fraction of the penetrant $\phi_p = \frac{\pi d^3 N_p}{6V}$ is kept below $\phi_p = 0.01$ to

ensure that the addition of penetrants will not affect network dynamics and to prevent significant interactions between penetrant molecules.

Standard dimensionless simulation quantities are employed,^{36,41} and denoted with tildes (e.g. $\tilde{T} = T/T^*$). Quantities are rendered dimensionless by several characteristic values: lengths are related to the bead diameter σ , energies are related to the thermal energy $k_B T^*$, and times are related to a time scale $\tau^* = \sqrt{m\sigma^2/k_B T^*}$, where m is the monomer mass. The characteristic temperatures T^* corresponds to 485 K, which is determined from parametrization against experiments,³⁵ using crosslinked poly(n-butyl acrylate) (PnBA) as a representative polymer that has been used by our experimental collaborators (see details in ref. 35).

Our MD simulations consider standard potentials for coarse-grained bead-spring polymers,⁴² including a Lennard-Jones potential \tilde{U}_{LJ} between all non-bonded beads, and both bonding \tilde{U}_B and bending \tilde{U}_θ potentials to model each semiflexible bead-spring chain. The overall energy is composed of a sum of these contributions:

$$\begin{aligned} \tilde{U} &= \tilde{U}_B + \tilde{U}_\theta + \tilde{U}_{LJ} \\ &= \sum_{i,j>i}^{N_{tot,n}} \tilde{u}_{B,ij} + \sum_{i,j>i,k>i,j}^{N_{tot,n}} \tilde{u}_{\theta,ijk} + \sum_{\alpha=n,p} \sum_{\beta=n,p} \sum_i^{N_{tot,\alpha}} \sum_{j>i}^{N_{tot,\beta}} \tilde{u}_{LJ,\alpha\beta,ij} \end{aligned} \quad (2)$$

Here the total system energy is written in terms of independent pairwise contributions $\tilde{u}_{B,\alpha,i}$, $\tilde{u}_{\theta,\alpha,i}$, and $\tilde{u}_{LJ,\alpha\beta,ij}$. Bonded monomers interact through harmonic bonding potential:

$$\tilde{u}_{B,ij} = \frac{\tilde{k}}{2} (\tilde{r}_{ij} - 1)^2 \Theta_{ij} \quad (3)$$

A large spring constant $\tilde{k} = 2000$ is adopted to enforce the equilibrium distance $\tilde{r}_{ij} = 1$ between bonded beads i and j . The factor Θ_{ij} determines the connectivity between monomer pairs, with

$\Theta_{ij} = 1$ being connected and $\Theta_{ij} = 0$ being disconnected; these values depend on the specific network that is formed. A bending energy is similarly introduced to account for chain stiffness:

$$\tilde{u}_{\theta,ijk} = \tilde{k}_{\theta}[1 - \cos\theta_{ijk}]\Theta_{ijk} \quad (4)$$

Here, the bond angle is between three adjacent beads i , j , and k whose connectivity is determined by a similar factor Θ_{ijk} to the one used for the bonding potential. The bending constant $\tilde{k}_{\theta} = 1.52$ is selected to reflect the experimental Kuhn length of PnBA.⁴³⁻⁴⁶ Further details of the parametrization are given in the literature.³⁵ A Lennard-Jones (LJ) potential is used to describe all non-bonded interactions between particles i and j on species α and β :

$$\tilde{u}_{\text{LJ},\alpha\beta,ij} = \begin{cases} 4\tilde{\epsilon}_{\alpha\beta} \left[\left(\frac{\tilde{d}_{\alpha} + \tilde{d}_{\beta}}{2\tilde{r}_{\alpha\beta}} \right)^{12} - \left(\frac{\tilde{d}_{\alpha} + \tilde{d}_{\beta}}{2\tilde{r}_{\alpha\beta}} \right)^6 \right], & \tilde{r}_{\alpha\beta} < \tilde{r}_{\text{cut}} = 2.5 \times \frac{\tilde{d}_{\alpha} + \tilde{d}_{\beta}}{2} \\ 0, & \text{otherwise} \end{cases} \quad (5)$$

Here, $\alpha, \beta \in \{\text{n}, \text{p}\}$, denotes the species as either network (n) or penetrant (p), with n denoting the monomer bead in the network and p denotes the penetrant. In the overall summation, $N_{\text{tot},n} = N_c N_m$ is the total number of network beads and $N_{\text{tot},p} = N_p$ is the total number of penetrant beads. The monomer size $\tilde{d}_n = 1$ is always unity (i.e., $d_n = \sigma$) and the penetrant size $\tilde{d}_p \equiv \tilde{d}$ is an important parameter for this study. In this study, we do not consider specific penetrant-polymer attractions, so keep $\tilde{\epsilon}_{nn} = \tilde{\epsilon}_{np} = \tilde{\epsilon}_{pp} = 1$.

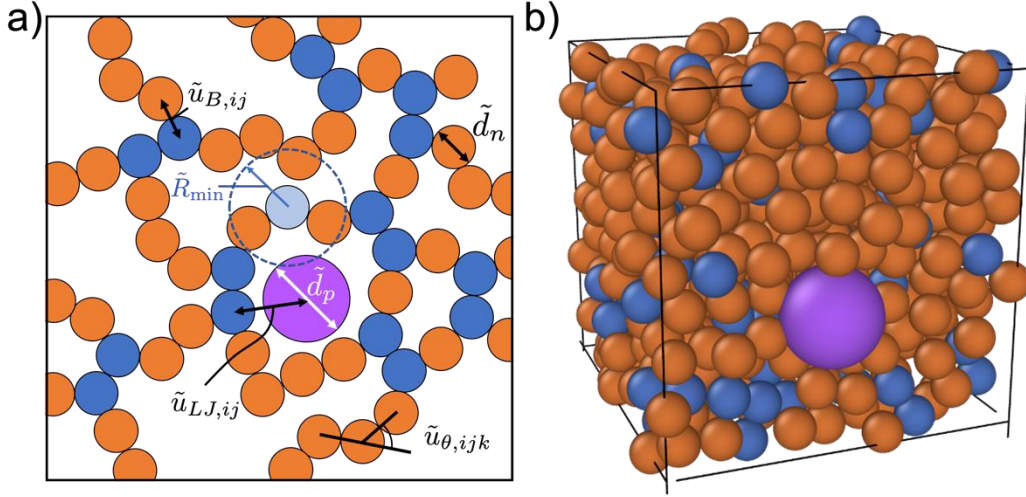


Figure 1. (a) Schematic illustrating the setup of our simulation. Monomer beads (orange) and crosslinker beads (blue) interact via bonding ($\tilde{u}_{B,ij}$) and angle ($\tilde{u}_{\theta,ijk}$) potentials, and can interact with each other and with the penetrant through Lennard-Jones potentials ($\tilde{u}_{LJ,ij}$). Monomer and crosslinker beads have a diameter $\tilde{d}_n = \sigma$ and the penetrant has a diameter \tilde{d}_p . Crosslinking occurs during an initial simulation step where ‘reactive’ beads (light blue) will form bonds with regular monomers within a cutoff distance \tilde{R}_{\min} . (b) Snapshot of a typical simulation, for $d/\sigma = 2.0$ and $f_{cross} = 0.11$.

The system is first equilibrated at $\tilde{T} = 1$, $\tilde{P} = 0$, and then networks are prepared by crosslinking the linear chains with reactive beads randomly distributed along the chain.^{35,47,48} The total number of reactive beads is $N_r = f_r N_m N_c$, where f_r is the fraction of reactive beads which tunes the crosslink density of networks. If the distance between a reactive bead and a free bead (orange beads in **Figure 1**) is within $\tilde{R}_{\min} = 1.1$, a new permanent bond will be formed given an assigned probability. Once a reactive bead forms a bond with a free bead, both the reactive bead and the free bead are labeled as crosslink beads (dark blue beads in **Figure 1**) and these two beads represent one crosslink ‘molecule’, in a way that reflects the specific chemistry used to synthesize PnBA networks,²¹ where the crosslinker molecular weight is roughly twice of the molecular weight of nBA. Crosslinking reactions were turned off once every reactive bead has formed a new bond with another free monomer (maximum number of possible bonds has been reached). In the end,

N_r reactive beads have reacted with the N_r free beads and they turned into $2N_r$ crosslink beads and belong to the N_r crosslink molecules. The crosslink density, f_{cross} , of networks is defined as:³⁵

$$f_{\text{cross}} = \frac{n_{\text{crosslink}}}{n_{\text{crosslink}} + n_{\text{monomer}}} = \frac{N_r}{N_m N_c - N_r} \quad (6)$$

Here, $n_{\text{crosslink}}$ and n_{monomer} are the number of crosslink molecules and nBA monomers, respectively. Four values of crosslink fraction f_{cross} are considered: 0.11, 0.25, 0.36, and 0.5.

After crosslinking, the system is cooled to a target temperature at a cooling rate $\tilde{T} = 8.3 \times 10^{-6}$ (corresponding to $\Gamma = 1.25 \times 10^9$ K/s in experimental units) and further equilibrated at constant $\tilde{P} = 0$. Another short NPT run was performed and the mean volume V is measured. We then switch to a NVT ensemble by setting the system volume to the mean volume V and equilibrate the system before final production run at NVT. All simulations are performed in LAMMPS⁴⁹ with a standard Nosé-Hoover thermostat and barostat.^{36,50,51}

The polymer network is characterized by its mesh size ($\tilde{\alpha}_x$), Kuhn segment alpha relaxation time ($\tilde{\tau}_{\alpha,K}$), and glass transition temperature T_g . The mesh size of networks at different crosslink densities is defined as the averaged distance between two adjacent crosslink beads on the same chain, and is tabulated in **Table S1**. The value of $\tilde{\tau}_{\alpha,K}$ at each temperature and crosslink density was defined as the time where the temporal autocorrelation function of a Kuhn monomer vector, $C_\lambda(\tilde{t}) = \langle P_2(\tilde{\mathbf{r}}_3(\tilde{t}) \cdot \tilde{\mathbf{r}}_3(0)) \rangle$ decays to $C_\lambda(\tilde{t}_{\text{max}}) + (1 - C_\lambda(\tilde{t}_{\text{max}}))/e$, where $C_\lambda(\tilde{t}_{\text{max}})$ represents the plateau value at the long-time limit \tilde{t}_{max} .⁵²⁻⁵⁶ Here, P_2 is the second Legendre polynomial and $\tilde{\mathbf{r}}_3$ is a vector between two beads that are 3 bonds apart which reflects the choice of coarse-grained bead relate to Kuhn segment of PnBA. T_g is then defined as when the Kuhn segment alpha relaxation time is $\tilde{\tau}_{\alpha,K}(\tilde{T}_g) = 10^5$. More information can be found in our previous work.³⁵

We characterize the dynamics of the penetrant motion by its alpha relaxation time, $\tilde{\tau}_{\alpha,p}$, and its diffusion coefficient D_p . To calculate $\tilde{\tau}_{\alpha,p}$, we use the self-intermediate scattering function (ISF) of the penetrant, which is given by:⁵³

$$F_s(\tilde{\mathbf{q}}, \tilde{t}) = \frac{1}{N_p} \sum_j^{N_p} \left\langle \exp \left[-i\tilde{\mathbf{q}} \cdot \left(\tilde{\mathbf{r}}_{pj}(\tilde{t}) - \tilde{\mathbf{r}}_{pj}(0) \right) \right] \right\rangle \quad (7)$$

where $\tilde{\mathbf{r}}_{pj}$ is the position of the j^{th} penetrant at time \tilde{t} , and $|\tilde{\mathbf{q}}|$ is set to the position of the first peak of the static structure factor for the networks, corresponding to $|\tilde{\mathbf{q}}| = 7.2$. The value of $\tilde{\tau}_{\alpha,p}$, is defined as the time required for $F_s(\tilde{\mathbf{q}}, \tilde{t})$ to decay to either $1/e$ or 0.1 from its initial ($\tilde{t} = 0$) value of unity. We characterize the mean-squared displacement (MSD) as a function of time: $\text{MSD}(\tilde{t}) = \langle \tilde{r}_p^2(\tilde{t}) \rangle = \frac{1}{N_p} \sum_j^{N_p} \left\langle \left(\tilde{\mathbf{r}}_{pj}(\tilde{t}) - \tilde{\mathbf{r}}_{pj}(0) \right)^2 \right\rangle$. The diffusion coefficient of penetrant is then obtained via the Einstein relation in the diffusive regime, $D_p = \lim_{\tilde{t} \rightarrow \infty} \frac{1}{6\tilde{t}} \langle \tilde{r}_p^2(\tilde{t}) \rangle$.⁵⁷

Results and Discussion

Penetrant Hopping and Diffusion in Dense Networks

We first characterize the diffusive motion of penetrants in polymer networks by studying the mean square displacement, $\langle \tilde{r}_p^2(\tilde{t}) \rangle$, of both small ($d/\sigma = 1.0$) and large ($d/\sigma = 2.0$) penetrants. The choice of these two particle sizes is motivated by considering particle sizes characteristic of model experimental systems in previous work by some of the authors,²² using PnBA as our representative network polymer (coarse-grained so that $\sigma = 0.573\text{nm}$), the span $d/\sigma \sim 1 - 2$ is typical for the average size of molecular penetrants.²² This choice also corresponds to the general length scale of the mesh size in the literature, which here ranges size from $\tilde{a}_x \sim 1.3 - 2.5$ (see **Table S1**). The MSD versus time \tilde{t} is plotted for both particle sizes in Figures 2a and 2b for $d/\sigma = 1.0$ and $d/\sigma = 2.0$ respectively, varying both the crosslink density f_{cross} and

temperature T . These plots show typical features characteristic of molecular diffusion. At short times, the particle exhibits ballistic motion such that the MSD scales as $\langle \tilde{r}_p^2(\tilde{t}) \rangle \sim \tilde{t}^2$; however, this regime gives way to a subdiffusive regime that we attribute to molecular caging by neighboring network monomers. At long times, the particle can overcome the barrier imposed by these cages, along with any constraints due to the network mesh, and undergo Fickian diffusion where $\langle \tilde{r}_p^2(\tilde{t}) \rangle \sim \tilde{t}^1$. These general features of diffusive motion are observed for both penetrant sizes and all crosslink densities and temperatures, however the specifics of penetrant caging and diffusive motion will be affected by these parameters.

The subdiffusive regime following the initial, ballistic penetrant motion provides insight into the time scales of caging, and large differences in the persistence of this regime are observed as f_{cross} , T , and d/σ are varied. To characterize this regime, we plot in **Figure S1** the slope of the MSD versus \tilde{t} curve on a log-log plot ($\beta = d \log \langle \tilde{r}_p^2(t) \rangle / d \log \tilde{t}$) as a function of time \tilde{t} . The minimum value of β is an estimate for the time \tilde{t}_β at which the penetrant is maximally subdiffusive or caged, and the value of $\langle \tilde{r}_p^2(\tilde{t}_\beta) \rangle^{1/2}$ correspondingly quantifies a transient localization length. A representative quantity is indicated in **Figures 2a** and **2b** with an open square, showing the caging onset for $\tilde{T} = 0.62$ and $f_{cross} = 0.25$. We only indicate a single representative value for each particle size, because the displacement $\langle \tilde{r}_p^2(\tilde{t}_\beta) \rangle^{1/2}$ is only weakly dependent on temperature and crosslink densities, and is far smaller than the length scale of the penetrant diameter ($\langle \tilde{r}_p^2(\tilde{t}_\beta) \rangle^{1/2} \sim 0.22$ for $d/\sigma = 1$ and $\langle \tilde{r}_p^2(\tilde{t}_\beta) \rangle^{1/2} \sim 0.32$ for $d/\sigma = 2$). This insensitivity leads us to interpret this onset of caging as tied to the structural correlations of the surrounding melt beads.

For both small ($d/\sigma = 1$) and large ($d/\sigma = 2$) penetrants, the value of $\beta \rightarrow 1$ at long times limits to Fickian behavior, however the time that it takes to reach this limit increases with decreasing temperature (**Figure 2** and **Figure S1**). This is the expected result of having less thermal energy to overcome the dynamic caging barrier,^{20,58} especially as our simulations approach the T_g . Similarly, an increase crosslink density f_{cross} monotonically increases the length of this subdiffusive regime and the minimum value of β concomitantly decreases (**Figure S2**) so that the MSD nearly exhibits a transient plateau. In principle, this is due to some combination of (1) an increase in the caging barrier because of the concomitant increase in the segmental relaxation time due to crosslinks³⁵ and (2) the impact of mesh confinement impeding penetrant motion.^{23,24,26} In this paper, a major result will be to show that the first interpretation is the dominant determinant of penetrant mobility for the models studied, especially as T_g is approached. This is apparent already by comparing the features in the MSD versus \tilde{t} to the mesh size $\tilde{\alpha}_x$, which were tabulated in **Table S1** for several different values of f_{cross} and indicated in **Figures 2** and **S1** as open circles. This length scale is often only accessed in or near the Fickian regime, suggesting that any effect on the subdiffusive transport of the penetrant in these simulations is subtle and not readily apparent from the MSD versus \tilde{t} plot alone. Despite this observation, it is apparent that both the temperature and crosslink density effects still depend on the penetrant size, with more pronounced changes in the subdiffusive regime for the larger ($d/\sigma = 2$) penetrants than the smaller ($d/\sigma = 1$) penetrants as T and f_{cross} are varied.

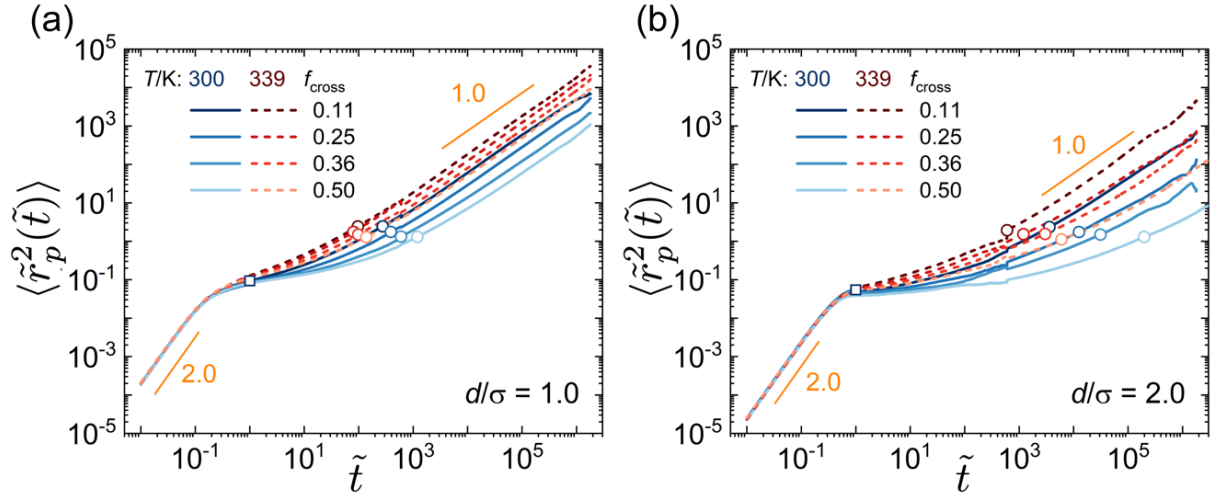


Figure 2. Mean square displacement $\langle \tilde{r}_p^2(\tilde{t}) \rangle$ versus time \tilde{t} of a penetrant particle with sizes (a) $d/\sigma = 1.0$ and (b) $d/\sigma = 2.0$, for several values of T and f_{cross} . Open squares denote a representative location for the onset of caging or transient localization, defined as the minimum slope β on this plot (see **Figure S1**) and chosen for $T = 300\text{K}$ and $f_{cross} = 0.11$. The analogous point for other values of T and f_{cross} would be almost identical. The open circles denote the length scale of the polymer network mesh size, as described in **Table S1**. The long-time data Fickian region, where the slope of this plot $\beta = 1$, is used to determine the penetrant diffusion constant \tilde{D}_p .

The MSD provides a molecular measure of penetrant transport, with the long-time Fickian regime providing an estimate of the overall diffusion coefficient \tilde{D}_p of the penetrant. However, this quantity is informed by the cumulative effect of both local particle motions as well as any larger length-scale transport effects of the network mesh confinement. To deconvolute these contributions, we also consider the time evolution of the self-ISF $F_s(\tilde{q}, \tilde{t})$ in **Figure 3**. Here we select a value $\tilde{q} = 7.2$ that is chosen to reflect the local structural cage of the polymer network and *not* the length scale of the network mesh. The curves shown in **Figure 3** thus only account for the dynamics of local relaxation and hopping, and quantify the extent to which the penetrant remains within its original cage. The first part of this decay is independent of temperature and crosslinking, and corresponds to the initial ballistic motion of the penetrant observed in **Figure 2**. There are

some subtle differences between the different penetrant sizes ($d/\sigma = 1.0$ vs. 2.0) that we attribute to the different masses of the penetrants and is also apparent in Figure 2.

At longer times, the decay of $F_s(\mathbf{q}, \tilde{t})$ becomes strongly dependent on temperature, crosslinking, and penetrant size in a manner consistent with the diffusive motion in **Figure 2**. At high temperatures, the smaller penetrant (**Figure 3a**) exhibits a non-exponential, long tail of $F_s(\mathbf{q}, \tilde{t})$ that we attribute to an activated but relatively rapid hopping process for penetrant relaxation. As crosslinking increases, this long-time tail extends further, and its non-exponential character becomes more pronounced. This trend is exacerbated by going to lower temperatures. We find there is a significant slowing down of penetrant motion even at intermediate times; this occurs around $\tilde{t} \sim 1$, which is roughly when the minimum in the apparent exponent β occurs for the MSD curves (in **Figure 2** and **S1**) and is consistent with the interpretation of this as the onset of penetrant caging. For larger penetrants ($d/\sigma = 2.0$, **Figure 3b**) this slowing down leads to the near-arrest of particle motion, again at $\tilde{t} \sim 1$, as evidenced by a plateau in $F_s(\mathbf{q}, \tilde{t})$ that only begins to relax at significantly longer times as the temperature is decreased or crosslinking fraction is increased. In both cases, we can attribute this arrest to the slow segmental relaxation dynamics of the surrounding network, as $F_s(\mathbf{q}, \tilde{t})$ is a local measure of hopping that does not probe the length scales relevant for mesh confinement.

The trends seen in the intermediate scattering function plots in **Figure 3** are largely consistent with those of the MSD plots in **Figure 2**, however we note several important differences that we will use to understand the mechanisms of penetrant motion in polymer networks. First, we note the similarity of the MSD versus time plots in **Figure 2a** for low temperatures and crosslink density ($T = 300\text{K}$ and $f_{cross} = 0.11$) and the high temperatures and crosslink density ($T = 339\text{K}$ and $f_{cross} = 0.36$); these curves almost overlap, and exhibit essentially the same diffusive

properties. Yet, the shapes of these curves in **Figure 3a** are distinctly different, with the characteristics of local caging more apparent in the lower temperature curve. In addition, there is a distinct difference in the subdiffusive regimes seen in the MSD plots versus $F_s(\mathbf{q}, \tilde{t})$, which are much more pronounced. This is contrast to normal glass-forming liquids, for which the same supercooling degree exhibits a weaker or shorter caging regime than for the MSD when compared to $F_s(\mathbf{q}, \tilde{t})$.^{59–66} These disparities between the MSD versus time and $F_s(\mathbf{q}, \tilde{t})$ suggest that mesh confinement may contribute meaningfully to the transport of penetrants in tight networks, and we seek to refine our physical understanding of this complicated interplay of local and long-time penetrant and network dynamics.

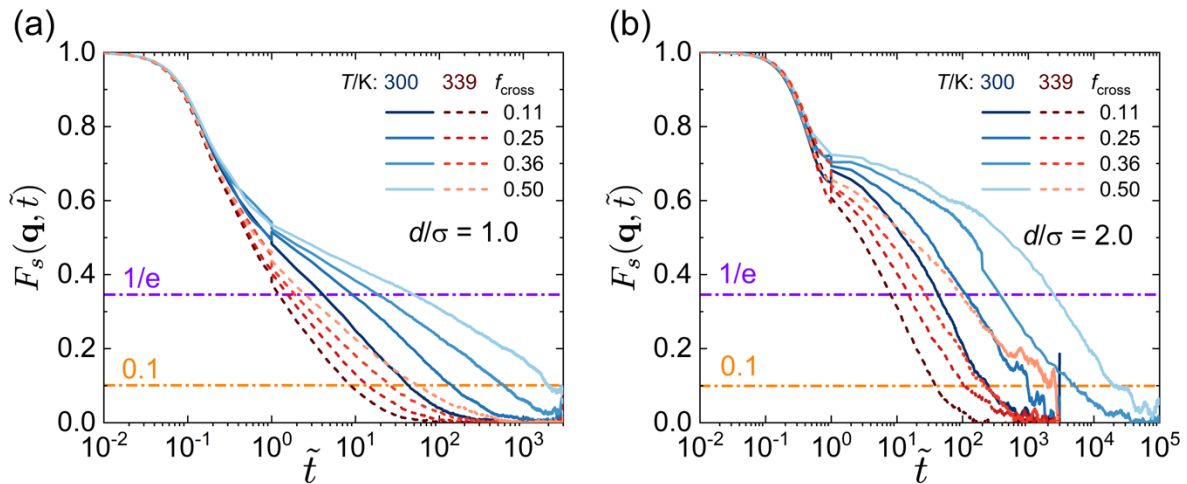


Figure 3. Intermediate scattering function $F_s(\mathbf{q}, \tilde{t})$ of the penetrant particle with (a) $d/\sigma = 1.0$ and (b) $d/\sigma = 2.0$ with $|\mathbf{q}| = 7.2$ at $T = 300\text{K}$ (solid, blue) and 339K (dashed, gray) for a variety of crosslink densities f_{cross} as a function of time \tilde{t} . The orange and purple horizontal lines define the penetrant alpha time, with the criteria $F_s(\mathbf{q}, \tau_{\alpha,p}) = 0.1$ and $F_s(\mathbf{q}, \tau_{\alpha,p'}) = 1/e$. The former criteria ($\tau_{\alpha,p}$) is more often used in this paper, because it includes the long tails observed in these functions that reflect a subpopulation of penetrants in long-lived cages. The latter criteria ($\tau_{\alpha,p'}$) may more closely relate to the average hopping time that is predicted in the theory developed in our companion paper, which does not account for dynamic heterogeneity and a distribution of penetrant hopping times.

Comparing the Role of Particle Size, Temperature, and Crosslinking on the Hopping and Diffusive Processes in Dense Networks

To quantify the relationship between local penetrant relaxation and diffusive motion, we extract the alpha time of the penetrant $\tilde{\tau}_{\alpha,p}$ from the ISF and the diffusion constant \tilde{D}_p from the MSD versus \tilde{t} . As described in the methods section, the diffusion constant is obtained from the long-time MSD curve via the expression $D_p = \lim_{t \rightarrow \infty} \frac{1}{6t} \langle \tilde{r}_p^2(\tilde{t}) \rangle$. The alpha time of the penetrant $\tilde{\tau}_{\alpha,p}$ is set from the decay of $F_s(\mathbf{q}, \tilde{t})$, and quantifies the time it takes to reach one of two possible criteria: $F_s(\mathbf{q}, \tilde{\tau}_{\alpha,p}) = 0.1$ and $F_s(\mathbf{q}, \tilde{\tau}_{\alpha,p'}) = 1/e$. While the specific criterion is arbitrary, these two criteria will be used to illustrate the effect of dynamic heterogeneity,^{65–68} the quantity $\tilde{\tau}_{\alpha,p}$ will account for the effect of the long-time tails in **Figure 3**, which do not contribute to the value $\tilde{\tau}_{\alpha,p'}$ that we deduce is closer to the average hopping time predicted in the accompanying theoretical work based on comparisons of the theory and simulation extracted relaxation times.⁶⁹ Differences between how $\tilde{\tau}_{\alpha,p}$ and $\tilde{\tau}_{\alpha,p'}$ depend on f_{cross} do depend on both T and d/σ , and as we will show can be very small or substantial. We will primarily report $\tilde{\tau}_{\alpha,p}$, considering $\tilde{\tau}_{\alpha,p'}$ only where the comparison is instructive. We can thus extract the key quantities in **Equation 1** directly from molecular simulations, the long-time diffusion \tilde{D}_p and the hopping time $\tilde{\tau}_{\alpha,p}$, and examine how they are related and affected by the state of the network and penetrant.

We start by considering $\tilde{\tau}_{\alpha,p}$, which we indicated in **Figure 3** and is typically between $\tilde{\tau}_{\alpha,p} = 10^1 - 10^3$ for $d/\sigma = 1.0$ and $\tilde{\tau}_{\alpha,p} = 10^1 - 10^4$ for $d/\sigma = 2.0$. Our goal is not to determine any precise dependence on d/σ , but rather to explore the differences between relatively ‘small’ and ‘large’ molecular penetrants in the context of experimental systems. We plot the inverse penetrant mean alpha times $1/\tilde{\tau}_{\alpha,p}$ or $1/\tilde{\tau}_{\alpha,p'}$ as a function of $T_g(f_{cross})/T$ for several

different temperatures T and crosslink fractions f_{cross} in **Figure 4**. We emphasize that the abscissa combines two parameters we consider in our model; the temperature T is plotted in different colors in all panels of **Figure 4a** and **b** for $d/\sigma = 1.0$ and $d/\sigma = 2.0$, respectively, and is directly set in our simulations. However, we note that T_g/T has multiple values for a given T due to the dependence of T_g on f_{cross} .³⁵ For the **Figure 4a** inset, we replot the data to show the corresponding plot of $1/\tilde{\tau}_{\alpha,p}$ versus T_g/T , but grouping data by f_{cross} instead of T .

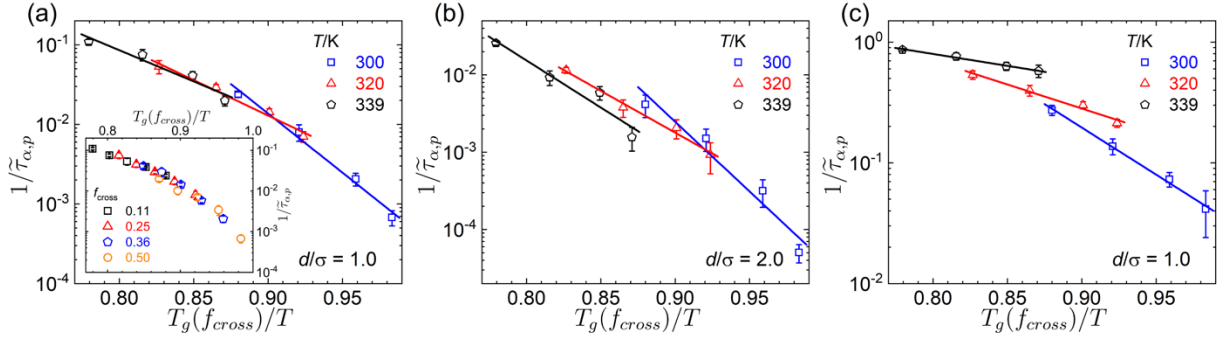


Figure 4. Inverse penetrant alpha time $1/\tilde{\tau}_{\alpha,p}$ calculated from simulations as a function of $T_g(f_{cross})/T$ for several temperatures T and penetrant sizes (a) $d/\sigma = 1.0$ and (b) $d/\sigma = 2.0$. In (a) there is a noticeable collapse to a single curve, which we illustrate more clearly in the inset by grouping with respect to f_{cross} . This collapse is no longer observed in (b). We also plot the shorter-time criteria for the penetrant alpha time $1/\tilde{\tau}_{\alpha,p'}$ versus $T_g(f_{cross})/T$ in (c) for $d/\sigma = 1.0$ to demonstrate that the coupling of penetrant hopping to crosslink density is noticeably weaker when the long-time tail in the intermediate scattering function is no longer included. The slopes of these plots are calculated and included in **Table 1**.

Figures 4a and **b** show that at a fixed T , the penetrant alpha relaxation time $1/\tilde{\tau}_{\alpha,p}$ behaves exponentially with $T_g(f_{cross})$, exhibiting Arrhenius-like behavior for both penetrant sizes. As the temperature increases, the absolute value of the slope of this curve decreases, demonstrating a stronger contribution from crosslink-induced T_g enhancement at lower temperatures. This underscores the importance of the network segmental dynamics on penetrant diffusion, and can be quantified by a change in the apparent activation energy that is proportional to the slope $\log \tilde{\tau}_{\alpha,p}$

versus T_g/T . To highlight how the choice of criterion $F_s(\mathbf{q}, \tilde{\tau}_{\alpha,p}) = 0.1$ affects our results, we plot in **Figure 4c** how **Figure 4a** would be changed upon choosing the alternative criterion, $F_s(\mathbf{q}, \tilde{\tau}_{\alpha,p'}) = 1/e$. In this case, similar trends are observed (i.e. an increasing apparent activation energy with decreasing temperature), however the magnitudes of the slopes are significantly smaller. We speculate that this is due to the neglect of longer time-scale processes that are apparent in the extended tails seen in **Figure 3**, meaning that the $1/e$ criterion does not fully capture the hopping processes thereby justifying our use of the 0.1 criterion. For both criteria and penetrant sizes d/σ , the values for the slopes of $\log \tilde{\tau}_{\alpha,p}$ versus T_g/T are calculated and tabulated in **Table 1** for different values of T . We note that for both penetrant sizes, these slopes exhibit similar trends to the predictions from theory in our companion paper, showing a modest decrease in the magnitude of the slope with increasing temperature for both $\tilde{\tau}_{\alpha,p}$ and $\tilde{\tau}_{\alpha,p'}$. However, the magnitudes of the slopes are significantly larger for $\tilde{\tau}_{\alpha,p}$ than the slopes for $\tilde{\tau}_{\alpha,p'}$, with the latter values in parenthesis in **Table 1**. We attribute this to the inclusion of the long-time tails of the ISF in $\tilde{\tau}_{\alpha,p}$, which indicate that penetrant hopping is influenced by dynamic heterogeneity near T_g due to the slower relaxation of a significant fraction (~ 5 - 10%) of particles.⁶⁶ To contrast, the long-time tails (dynamic heterogeneity) do not (or weakly/negligibly) affect $\tilde{\tau}_{\alpha,p'}$, leading to a weaker apparent coupling between the near- T_g dynamics of the network and the penetrant hopping.

Table 1. Slope for $\log \tilde{\tau}_{\alpha,p}$ or \tilde{D}_p^{-1} versus T_g/T from simulations at several temperatures ($T = 300, 320, \text{ and } 339\text{K}$) and penetrant sizes ($d/\sigma = 1$ and 2). Both criteria $\tilde{\tau}_{\alpha,p}$ and $\tilde{\tau}_{\alpha,p'}$ (in parentheses) are considered.

T/K	d/σ	300	320	339
$\log(\tilde{\tau}_{\alpha,p})$ vs T_g/T	1.0	15.57 (7.79)	8.59 (3.98)	8.01 (1.97)
$\log(1/D_p)$ vs T_g/T	1.0	9.34	7.48	5.79
$\log(\tilde{\tau}_{\alpha,p})$ vs T_g/T	2.0	18.13 (16.10)	12.86 (8.78)	14.80 (9.60)

log (1/D_p) vs T_g/T	2.0	17.47	19.27	18.12
---	-----	-------	-------	-------

The two different penetrant sizes in **Figure 4a** and **4b** exhibit similar trends, including nearly the same overall decrease of relaxation rate by a little over two decades (over all values of T and f_{cross}). However, there are subtle but important differences. At a fixed value of $T_g(f_{cross})/T$ (i.e. at a fixed supercooling degree), we observe that the penetrant alpha time is roughly constant with decreasing temperature for $d/\sigma = 1.0$. This lower temperature also corresponds to a lower degree of crosslinking f_{cross} . This means that the degree of supercooling $T_g(f_{cross})/T$ largely dictates penetrant hopping, with the absolute temperature T playing a similar role in affecting transport as the effective T_g . In this case, several effects – changing T_g , absolute T , and crosslinking (f_{cross}) – tend to cancel resulting in a near collapse of the $1/\tilde{\tau}_{\alpha,p}$ versus T_g/T data. This is highlighted in the inset of **Figure 4a**, which is the same data as in the main frame but grouped by f_{cross} instead of T , and more clearly shows how well this data collapses to a single curve. **Figure 4b** shows that this balance no longer holds for larger penetrants $d/\sigma = 2.0$, with lower T values exhibiting faster dynamics (i.e. higher $1/\tilde{\tau}_{\alpha,p}$) at a given degree of supercooling $T_g(f_{cross})/T$ due to the corresponding decrease in the f_{cross} .

This same competition is apparent in the diffusion constant \tilde{D}_p , which we plot in **Figure 5a** and **b** for $d/\sigma = 1.0$ and $d/\sigma = 2.0$ respectively, and at the same conditions plotted in **Figure 4a** and **b**. Like $1/\tilde{\tau}_{\alpha,p}$, \tilde{D}_p exhibits Arrhenius-like behavior as defined by a straight line on a $\log \tilde{D}_p$ versus T_g/T plot. The primary difference is in the relative magnitude change in D_p at different degrees of supercooling T_g/T . \tilde{D}_p still exhibits a near-collapse for $d/\sigma = 1.0$, however generally decreases more slowly than $1/\tilde{\tau}_{\alpha,p}$ in **Figure 4a**. For the larger penetrant size $d/\sigma = 2.0$, the situation is more complicated. In this case, high temperatures T in **Figure 5b** show a more

dramatic decrease in \tilde{D}_p with T_g/T than that of $1/\tilde{\tau}_{\alpha,p}$ in **Figure 4b**, but a similar decrease at lower temperatures. These effects are quantified by calculating the slope of the $-\log \tilde{D}_p$ versus T_g/T relationship, which we include in **Table 1** for both penetrant sizes. Here, the \tilde{D}_p slopes are significantly smaller than the $\tilde{\tau}_{\alpha,p}$ slopes for $d/\sigma = 1.0$, but are similar or larger than the $\tilde{\tau}_{\alpha,p}$ for $d/\sigma = 2.0$. The latter behavior for $d/\sigma = 2.0$ is qualitatively consistent with the results in our companion theory paper,⁶⁹ which finds that the diffusion constant \tilde{D}_p changes with supercooling T_g/T similarly or more pronounced than the corresponding inverse $\tilde{\tau}_{\alpha,p}$. For $d/\sigma = 1.0$, however, the theory predicts that the \tilde{D}_p slopes will be similar to inverse $\tilde{\tau}_{\alpha,p}$ slopes, in contrast to the simulation observation that the \tilde{D}_p slopes are much smaller. We attribute this disparity between simulation and theory to the larger importance of dynamic heterogeneity for smaller penetrants in our simulations,⁶⁶ because the theory only makes predictions for a mean penetrant alpha time that is closer to our value $\tilde{\tau}_{\alpha,p}$. Indeed, for $d/\sigma = 1.0$ the relative slopes for \tilde{D}_p and $1/\tilde{\tau}_{\alpha,p}$ calculated using this criterion (in parentheses in **Table 1**) are much more consistent with the theoretical predictions.⁶⁹

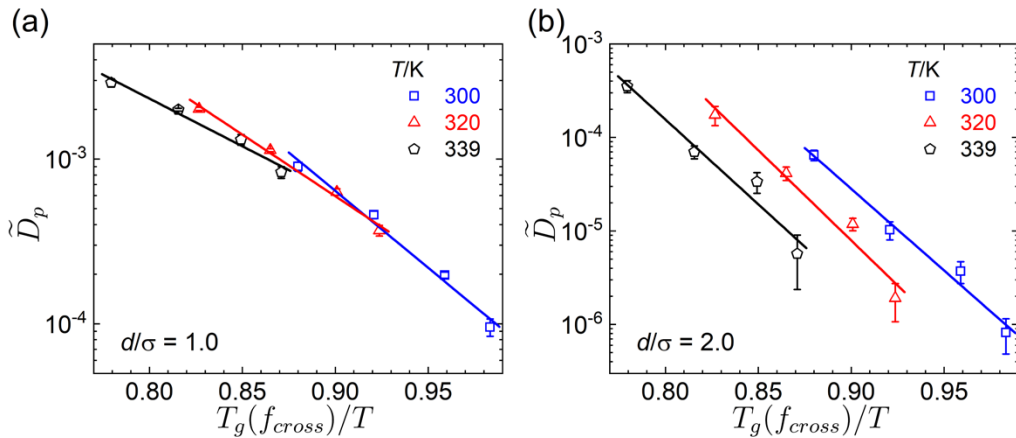


Figure 5. (a) Penetrant diffusion constant \tilde{D}_p as a function of $T_g(f_{cross})/T$ for several temperatures T and penetrant sizes (a) $d/\sigma = 1.0$ and (b) $d/\sigma = 2.0$. These are the same

conditions as in **Figure 4a** and **b**, and similarly there is a collapse in (a) that is no longer present in (b). The slopes of these plots are calculated and included in **Table 1**.

To contextualize the relationship between the diffusion constant \tilde{D}_p , inverse penetrant alpha time $1/\tilde{\tau}_{\alpha,p}$, temperature T , and particle size d/σ , we plot both \tilde{D}_p and $1/\tilde{\tau}_{\alpha,p}$ as a function of T_g/T in **Figure 6** for two temperatures each. We have used a multiplier A to align these data sets at the leftmost points, to compare how the effect of changing the crosslinking fraction f_{cross} (and concomitantly the T_g) on \tilde{D}_p versus $1/\tilde{\tau}_{\alpha,p}$. For small particles ($d/\sigma = 1.0$), the value of \tilde{D}_p exhibits a weaker decrease with the degree of supercooling T_g/T than $1/\tilde{\tau}_{\alpha,p}$ for both temperatures T . We believe that this is again a dynamic heterogeneity effect, which manifests as the well-known breakdown of the Stokes-Einstein relation in glassy liquids,^{59–66} where the diffusion constant is understood to be dominated by the subpopulation of particles undergoing rapid transport and is thus less dependent on T_g/T than the particle hopping time that characterizes a relaxation process.⁶⁶ To contrast, for larger particles ($d/\sigma = 2.0$) the change in the diffusion constant \tilde{D}_p tracks the change in $1/\tilde{\tau}_{\alpha,p}$ with increasing f_{cross} at low temperatures ($T = 300\text{K}$) and even decreases more than $1/\tilde{\tau}_{\alpha,p}$ with increasing f_{cross} at higher temperatures ($T = 339\text{K}$). This indicates that there is an additional mechanism slowing down diffusive penetrant motion at length scales longer than what is probed in the intermediate scattering function (the local molecular cage, $1/\tilde{\tau}_{\alpha,p}$), which we attribute to the effect of mesh confinement.

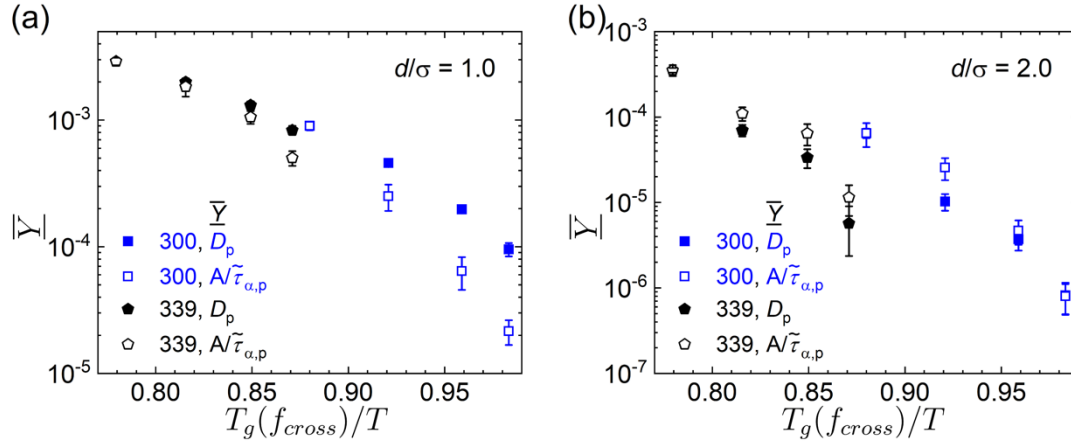


Figure 6. Comparison of the penetrant diffusion constant \tilde{D}_p and inverse penetrant alpha time $1/\tilde{\tau}_{\alpha,p}$ as a function of $T_g(f_{cross})/T$ at both high (339K) and a low (339K) temperatures for (a) $d/\sigma = 1.0$ and (b) $d/\sigma = 2.0$. $1/\tilde{\tau}_{\alpha,p}$ is vertically shifted down by a factor (a) $A = 3.40 \times 10^{-3}$ and (b) $A = 2.55 \times 10^{-3}$ such that the leftmost point of alpha time $1/\tilde{\tau}_{\alpha,p}$ at a given temperature coincides with the corresponding \tilde{D}_p data point for better comparison. In (a), this comparison shows that \tilde{D}_p exhibits a weaker dependence than $1/\tilde{\tau}_{\alpha,p}$ with $T_g(f_{cross})/T$ for all temperatures, while in (b) \tilde{D}_p exhibits a stronger dependence than $1/\tilde{\tau}_{\alpha,p}$ at high temperatures.

To isolate the role of mesh confinement, we refer to the form of **Equation 1** that writes the diffusion constant as the product of $1/\tilde{\tau}_{\alpha,p}$ and a mesh confinement factor X . The form predicted for X is model-dependent,^{23,24,26} but we can directly evaluate this quantity from simulation by taking the product $X = \tilde{D}_p \tilde{\tau}_{\alpha,p}$. We plot $\tilde{D}_p \tilde{\tau}_{\alpha,p}$ in **Figure 7** for both penetrant sizes as a function of T_g/T and T , in analogy with **Figures 4** and **5**. **Figure 7a** plots this product for small penetrants ($d/\sigma = 1.0$), and as expected from **Figures 4a** and **5a** the data roughly collapses to a single curve that increases monotonically with the degree of supercooling T_g/T . This trend is generically expected for one-component glass-forming liquids due to alpha process dynamic heterogeneity,⁶⁶ so in this case the network primarily affects penetrant transport through the dependence of T_g on f_{cross} . Notably, this monotonic increase in $\tilde{D}_p \tilde{\tau}_{\alpha,p}$ is no longer seen when the 1/e criterion is

considered (see inset to **Figure 7a**), demonstrating that the long-time tail in the ISF should be responsible for the behavior in the main panel of **Figure 7a**. To contrast, **Figure 7b** plots the product $\tilde{D}_p \tilde{\tau}_{\alpha,p}$ for larger penetrants ($d/\sigma = 2.0$), and exhibits a significant *decrease* with T_g/T for each of the higher temperatures $T = 339$ and 320 . For a constant temperature, the increase with T_g/T corresponds to an increase in both f_{cross} and C . We can thus attribute this dependence to the effect of mesh confinement (and also the reduced importance of glassy dynamic heterogeneity since larger particles tend to average over it), as this decrease of $\tilde{D}_p \tilde{\tau}_{\alpha,p} = X$ with C is predicted by both Cai, *et al.*²³ and Dell and Schweizer.²⁶ However, this trend is less noticeable for the lowest temperature $T = 300\text{K}$, where within error $\tilde{D}_p \tilde{\tau}_{\alpha,p}$ remains roughly constant. The expected increase in $\tilde{D}_p \tilde{\tau}_{\alpha,p}$ for glassy melts appears to cancel out any mesh confinement effects, indicating that the local caging and mesh confinement both contribute to penetrant dynamics in this limit.

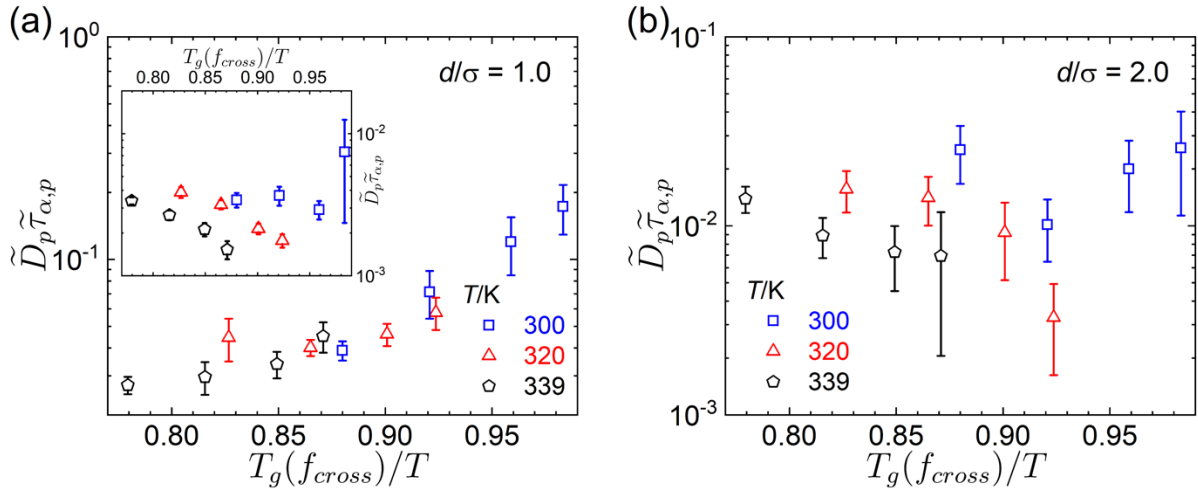


Figure 7. The product $\tilde{D}_p \tilde{\tau}_{\alpha,p}$ as a function of $T_g(f_{cross})/T$ for several temperatures T for (a) $d/\sigma = 1.0$ and (b) $d/\sigma = 2.0$ with the 0.1 criterion. For (a) there is a collapse to an increasing curve that reflects the breakdown of Stokes-Einstein that is characteristic of dynamic heterogeneity in glass forming liquids. The inset shows the same plot, but using the 1/e criterion. For (b) at high temperatures, each temperature exhibits a monotonic decrease in the product $\tilde{D}_p \tilde{\tau}_{\alpha,p}$ that we attribute to the effect of mesh confinement. At low temperatures ($T = 300\text{K}$) and $d/\sigma = 2.0$, the

increase due to dynamic heterogeneity appears to counteract the effect of mesh confinement, leading to a roughly constant value of $\tilde{D}_p \tilde{\tau}_{\alpha,p}$.

Network and Penetrant Dynamic Decoupling and Particle Size

We quantified penetrant dynamics, determining both the local hopping via $1/\tilde{\tau}_{\alpha,p}$ and the long-time diffusion via \tilde{D}_p . These results demonstrated that (1) both processes were primarily governed by local network segmental motion (i.e. glass physics) at low temperatures, yet (2) crosslinks nevertheless had a more pronounced effect on \tilde{D}_p for larger penetrants ($d/\sigma = 2.0$ versus $d/\sigma = 1.0$ in **Table 1**). To understand these two observations, we quantify the coupling between the penetrant alpha time $\tilde{\tau}_{\alpha,p'}$ and the network alpha relaxation time $\tilde{\tau}_{\alpha,K}$, where the latter is obtained from the autocorrelation function of the Kuhn monomer vector per our prior work.³⁵ In this case, we use the short-time criterion $\tilde{\tau}_{\alpha,p'}$ due to its better consistency with both the theoretical predictions and to match the $1/e$ criterion used in calculating $\tilde{\tau}_{\alpha,K}$ previously. The ratio between these two properties $\tilde{\tau}_{\alpha,p'}/\tilde{\tau}_{\alpha,K}$ is plotted as a function of T_g/T in **Figure 8** for both penetrant sizes and all temperatures T studied; this comparison has previously demonstrated to be useful in the self-consistent cooperative hopping (SCCH) theory of hard sphere mixtures and dilute penetrants in polymer melts,^{20,58,70} and quantifies the degree of ‘dynamic coupling/decoupling’. In these previous theories, the ratio $\tilde{\tau}_{\alpha,p'}/\tilde{\tau}_{\alpha,K}$ was measured in the context of ‘packing fraction’, which is qualitatively analogous to inverse temperature.⁵⁸ The theory predicted that the ratio $\tilde{\tau}_{\alpha,p'}/\tilde{\tau}_{\alpha,K}$ (1) initially increases slightly as the temperature is lowered from high temperature, and then (2) sharply decreases in a penetrant size-dependent manner (stronger decrease for smaller penetrants) as temperature is further lowered towards the glassy state.^{58,69} This indicates a strong decoupling between penetrant and matrix dynamics.

In **Figure 8**, both penetrants show only a modest dependence of $\tilde{\tau}_{\alpha,p'}/\tilde{\tau}_{\alpha,K}$ on T_g/T , spanning only roughly a decade in the simulation-accessible weakly supercooled regime. We do not observe the characteristic decrease in $\tilde{\tau}_{\alpha,p'}/\tilde{\tau}_{\alpha,K}$ predicted for the deeply supercooled regime, which is expected to be computationally inaccessible, though our trends are consistent with the weak changes in $\tilde{\tau}_{\alpha,p'}/\tilde{\tau}_{\alpha,K}$ predicted by the theory in the polymer alpha relaxation time range probed in our simulation.⁶⁹ Importantly, the relative magnitude of these ratios is instructive. $\tilde{\tau}_{\alpha,p}/\tilde{\tau}_{\alpha,K}$ for the $d/\sigma = 2.0$ penetrant is at least an order of magnitude larger than that for the $d/\sigma = 1.0$ penetrant, indicating that it is more strongly coupled to the surrounding matrix as generically expected and as predicted by SCCH theory. This helps explain our results for $1/\tilde{\tau}_{\alpha,p}$ and \tilde{D}_p in the previous section; in those results, there was a stronger dependence of \tilde{D}_p for the larger penetrants on f_{cross} even at lower temperatures where mesh confinement is not dominant (see **Table 1**). We can now attribute this to the stronger matrix-penetrant coupling for larger penetrants, rather than enhanced mesh confinement.

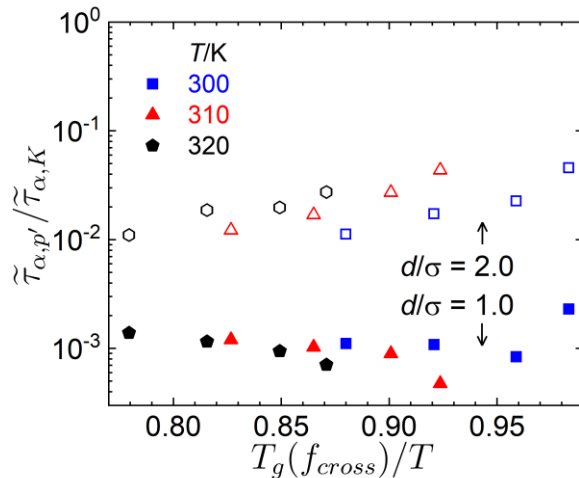


Figure 8. Degree of decoupling between penetrant and Kuhn segment dynamics, as quantified by the ratio $\tilde{\tau}_{\alpha,p'}/\tilde{\tau}_{\alpha,K}$, as a function of $T_g(f_{cross})/T$ for several temperatures and both $d/\sigma = 1.0$ and $d/\sigma = 2.0$. While the trends with $T_g(f_{cross})/T$ are quite weak, the larger penetrant $d/\sigma = 2.0$

couples significantly more strongly to the segmental dynamics of the surrounding network, as evident in the order-of-magnitude larger value of $\tilde{\tau}_{\alpha,p}/\tilde{\tau}_{\alpha,K}$ when compared to the smaller penetrant $d/\sigma = 1.0$.

Degeneracy of Mesh Size Effects Due to Confinement and Glassy Dynamics

From a molecular viewpoint, we only see significant mesh confinement effects on penetrant diffusion in the limit of large particles and high temperatures, and for small molecules or low temperatures show that crosslinking instead impacts penetrant diffusion primarily through its effect on the local segmental relaxation of the polymer matrix. However, even in this limit we can demonstrate results consistent with aspects of **Equation 1** if we plot our data versus the confinement ratio C rather than the extent of supercooling T_g/T . We consider two candidate models for X , by plotting CD_p versus C^2 in **Figure 9a** based on the predictions of Cai, *et al.*²³ and \tilde{D}_p versus C in **Figure 9b** based on the predictions of Dell and Schweizer.²⁶ Despite already demonstrating that mesh confinement does *not* play a significant role for small penetrants, these plots exhibit remarkably good agreement with the functional forms predicted by both models as indicated by the nearly linear trends in these semi-log plots. However, there is a non-negligible change in slope in both plots of **Figure 9** as the temperature T is changed, which is not a prediction for either entropic mesh confinement model.^{23,25,26} As per **Equation 1**, these models that only have a temperature dependence in the prefactor $1/\tau_{\alpha,p}$ (plotted also versus C from simulation in **Figure S2**) and not in the exponent of the entropic mesh confinement factor X . This key observation allows the effects of crosslinking on the penetrant relaxation time to be distinguished from the effects of crosslinking due to mesh confinement, in the absence of simulation determination of $1/\tau_{\alpha,p}$, though this distinguishing feature may become weak as in the case of larger penetrants as is shown in the supporting information ($d/\sigma = 2.0$, **Figure S3**).

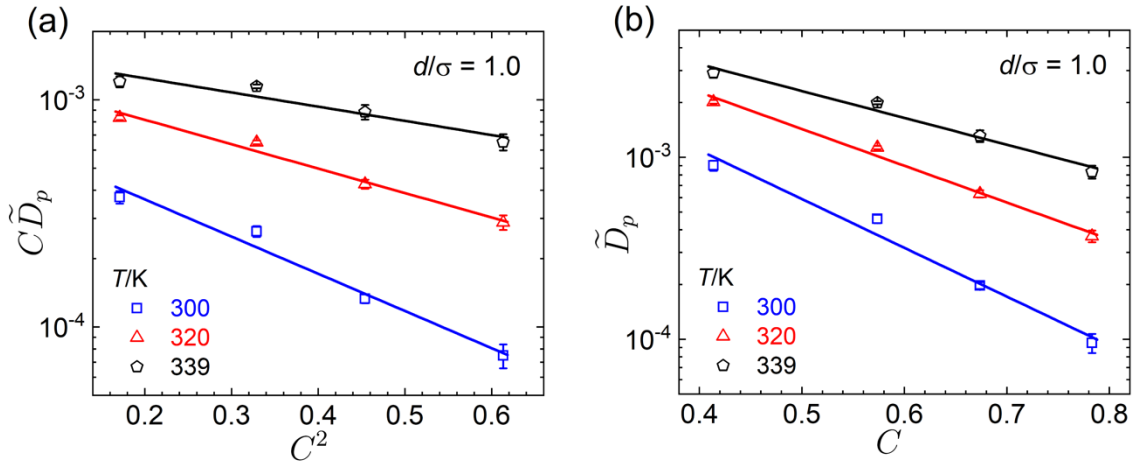


Figure 9. The penetrant diffusion constant \tilde{D}_p plotted with respect to the confinement ratio C as suggested by the forms of various literature predictions for mesh confinement effects. (a) Cai, *et al.*²³ predicts that $\tilde{D}_p \propto C^{-1} \exp(-C^2)$ and (b) Dell and Schweizer²⁶ predict that $\tilde{D}_p \propto \exp(-bC)$. Both ways of plotting this data appear linear, even though mesh confinement does not play a major role in penetrant transport for the $d/\sigma = 1.0$ case plotted here. The main indication that the simulations do *not* agree with the idea that entropic mesh confinement is dominant lie in the temperature-dependent slopes, which for mesh confinement should not change with temperature.

Conclusion

In this paper, we used simulation to understand the role of glassy dynamics versus mesh confinement on the diffusion and alpha relaxation of molecular penetrants in polymer networks.

We consider a specific form for the diffusion constant, $D_p \sim (d^2/\tau_{\alpha,p})X$, that allows us to isolate the effect of network mesh confinement X through calculating and studying both the diffusion constant \tilde{D}_p and the penetrant hopping or alpha relaxation time $\tilde{\tau}_{\alpha,p}$. Both quantities exhibit Arrhenius-like trends with the degree of supercooling T_g/T at a fixed temperature, due to the dependence of T_g on the extent of crosslinking. This strong coupling between penetrant hopping and crosslinking-dependent glassy dynamics is consistent with theoretical predictions in the companion paper,⁶⁹ but also exhibits significant breakdown in the Stokes-Einstein relationship if a strong dynamic heterogeneity effect⁶⁵⁻⁶⁸ is apparent in the hopping dynamics of the smaller molecular penetrants as the system is supercooled to larger values of T_g/T .⁶⁶ For small penetrants,

the effect of crosslinking on T_g is demonstrated to dominate diffusive motion, with a collapse to a single dependence of both $\tilde{\tau}_{\alpha,p}$ and \tilde{D}_p on T_g/T . This collapse is no longer apparent for larger penetrants, where we show by plotting the product $\tilde{D}_p\tilde{\tau}_{\alpha,p}$ with T_g/T that we see the signatures of mesh confinement at low temperatures. While we show that crosslinking affects molecular penetrant transport through *both* its effect on T_g and through mesh confinement, the former appears to be the dominant mechanism for our simulations. We can also show, however, that the diffusion constant \tilde{D}_p still follows trends predicted in the literature for mesh confinement,^{23,24,26} due to a degeneracy of how crosslink fraction changes with T_g and mesh size as predicted by SCCH theory.⁶⁹ This underscores the difficulty of drawing conclusions on transport mechanisms from diffusion data alone.

Acknowledgement

This research was supported by the U.S. Department of Energy, Office of Basic Energy Sciences, Division of Materials Sciences and Engineering (Award No. DE-SC0020858), through the Materials Research Laboratory at the University of Illinois at Urbana-Champaign. Helpful discussions with Christopher Evans are gratefully acknowledged.

References:

- (1) Blaiszik, B. J.; Kramer, S. L. B.; Olugebefola, S. C.; Moore, J. S.; Sottos, N. R.; White, S. R. Self-Healing Polymers and Composites. *Annu. Rev. Mater. Res.* **2010**, *40* (1), 179–211. <https://doi.org/10.1146/annurev-matsci-070909-104532>.
- (2) Patrick, J. F.; Robb, M. J.; Sottos, N. R.; Moore, J. S.; White, S. R. Polymers with Autonomous Life-Cycle Control. *Nature* **2016**, *540* (7633), 363–370. <https://doi.org/10.1038/nature21002>.
- (3) Wang, H.; Keum, J. K.; Hiltner, A.; Baer, E.; Freeman, B.; Rozanski, A.; Galeski, A. Confined Crystallization of Polyethylene Oxide in Nanolayer Assemblies. *Science* **2009**, *323* (5915), 757–760. <https://doi.org/10.1126/science.1164601>.
- (4) Wang, C.; Ge, Q.; Ting, D.; Nguyen, D.; Shen, H.-R.; Chen, J.; Eisen, H. N.; Heller, J.; Langer, R.; Putnam, D. Molecularly Engineered Poly(Ortho Ester) Microspheres for

- Enhanced Delivery of DNA Vaccines. *Nat. Mater.* **2004**, *3* (3), 190–196. <https://doi.org/10.1038/nmat1075>.
- (5) Li, J.; Mooney, D. J. Designing Hydrogels for Controlled Drug Delivery. *Nat. Rev. Mater.* **2016**, *1* (12), 16071. <https://doi.org/10.1038/natrevmats.2016.71>.
 - (6) White, S. R.; Sottos, N. R.; Geubelle, P. H.; Moore, J. S.; Kessler, M. R.; Sriram, S. R.; Brown, E. N.; Viswanathan, S. Autonomic Healing of Polymer Composites. *Nature* **2001**, *409* (6822), 794–797. <https://doi.org/10.1038/35057232>.
 - (7) Galizia, M.; Chi, W. S.; Smith, Z. P.; Merkel, T. C.; Baker, R. W.; Freeman, B. D. *50th Anniversary Perspective*: Polymers and Mixed Matrix Membranes for Gas and Vapor Separation: A Review and Prospective Opportunities. *Macromolecules* **2017**, *50* (20), 7809–7843. <https://doi.org/10.1021/acs.macromol.7b01718>.
 - (8) Sanders, D. F.; Smith, Z. P.; Guo, R.; Robeson, L. M.; McGrath, J. E.; Paul, D. R.; Freeman, B. D. Energy-Efficient Polymeric Gas Separation Membranes for a Sustainable Future: A Review. *Polymer* **2013**, *54* (18), 4729–4761. <https://doi.org/10.1016/j.polymer.2013.05.075>.
 - (9) Lau, C. H.; Li, P.; Li, F.; Chung, T.-S.; Paul, D. R. Reverse-Selective Polymeric Membranes for Gas Separations. *Prog. Polym. Sci.* **2013**, *38* (5), 740–766. <https://doi.org/10.1016/j.progpolymsci.2012.09.006>.
 - (10) Low, Z.-X.; Budd, P. M.; McKeown, N. B.; Patterson, D. A. Gas Permeation Properties, Physical Aging, and Its Mitigation in High Free Volume Glassy Polymers. *Chem. Rev.* **2018**, *118* (12), 5871–5911. <https://doi.org/10.1021/acs.chemrev.7b00629>.
 - (11) Li, D.; Zhang, X.; Yao, J.; Simon, G. P.; Wang, H. Stimuli-Responsive Polymer Hydrogels as a New Class of Draw Agent for Forward Osmosis Desalination. *Chem. Commun.* **2011**, *47* (6), 1710. <https://doi.org/10.1039/c0cc04701e>.
 - (12) Geise, G. M.; Lee, H.-S.; Miller, D. J.; Freeman, B. D.; McGrath, J. E.; Paul, D. R. Water Purification by Membranes: The Role of Polymer Science. *J. Polym. Sci. Part B Polym. Phys.* **2010**, *48* (15), 1685–1718. <https://doi.org/10.1002/polb.22037>.
 - (13) Geise, G. M.; Paul, D. R.; Freeman, B. D. Fundamental Water and Salt Transport Properties of Polymeric Materials. *Prog. Polym. Sci.* **2014**, *39* (1), 1–42. <https://doi.org/10.1016/j.progpolymsci.2013.07.001>.
 - (14) Feng, X.; Huang, R. Y. M. Liquid Separation by Membrane Pervaporation: A Review. *Ind. Eng. Chem. Res.* **1997**, *36* (4), 1048–1066. <https://doi.org/10.1021/ie960189g>.
 - (15) Sholl, D. S.; Lively, R. P. Seven Chemical Separations to Change the World. *Nature* **2016**, *532* (7600), 435–437. <https://doi.org/10.1038/532435a>.
 - (16) Kosinov, N.; Gascon, J.; Kapteijn, F.; Hensen, E. J. M. Recent Developments in Zeolite Membranes for Gas Separation. *J. Membr. Sci.* **2016**, *499*, 65–79. <https://doi.org/10.1016/j.memsci.2015.10.049>.
 - (17) Trickett, C. A.; Helal, A.; Al-Maythaly, B. A.; Yamani, Z. H.; Cordova, K. E.; Yaghi, O. M. The Chemistry of Metal–Organic Frameworks for CO₂ Capture, Regeneration and Conversion. *Nat. Rev. Mater.* **2017**, *2* (8), 17045. <https://doi.org/10.1038/natrevmats.2017.45>.
 - (18) Qian, Q.; Asinger, P. A.; Lee, M. J.; Han, G.; Mizrahi Rodriguez, K.; Lin, S.; Benedetti, F. M.; Wu, A. X.; Chi, W. S.; Smith, Z. P. MOF-Based Membranes for Gas Separations. *Chem. Rev.* **2020**, *120* (16), 8161–8266. <https://doi.org/10.1021/acs.chemrev.0c00119>.
 - (19) Yuan, S.; Li, X.; Zhu, J.; Zhang, G.; Van Puyvelde, P.; Van der Bruggen, B. Covalent Organic Frameworks for Membrane Separation. *Chem. Soc. Rev.* **2019**, *48* (10), 2665–2681. <https://doi.org/10.1039/C8CS00919H>.

- (20) Mei, B.; Schweizer, K. S. Theory of the Effects of Specific Attractions and Chain Connectivity on the Activated Dynamics and Selective Transport of Penetrants in Polymer Melts. *Macromolecules* **2022**, *55* (20), 9134–9151. <https://doi.org/10.1021/acs.macromol.2c01549>.
- (21) Sheridan, G. S.; Evans, C. M. Understanding the Roles of Mesh Size, T_g , and Segmental Dynamics on Probe Diffusion in Dense Polymer Networks. *Macromolecules* **2021**, *54* (23), 11198–11208. <https://doi.org/10.1021/acs.macromol.1c01767>.
- (22) Mei, B.; Sheridan, G. S.; Evans, C. M.; Schweizer, K. S. Elucidation of the Physical Factors That Control Activated Transport of Penetrants in Chemically Complex Glass-Forming Liquids. *Proc. Natl. Acad. Sci.* **2022**, *119* (41), e2210094119. <https://doi.org/10.1073/pnas.2210094119>.
- (23) Cai, L.-H.; Panyukov, S.; Rubinstein, M. Hopping Diffusion of Nanoparticles in Polymer Matrices. *Macromolecules* **2015**, *48* (3), 847–862. <https://doi.org/10.1021/ma501608x>.
- (24) Sorichetti, V.; Hugouvieux, V.; Kob, W. Dynamics of Nanoparticles in Polydisperse Polymer Networks: From Free Diffusion to Hopping. *Macromolecules* **2021**, *54* (18), 8575–8589. <https://doi.org/10.1021/acs.macromol.1c01394>.
- (25) Xu, Z.; Dai, X.; Bu, X.; Yang, Y.; Zhang, X.; Man, X.; Zhang, X.; Doi, M.; Yan, L.-T. Enhanced Heterogeneous Diffusion of Nanoparticles in Semiflexible Networks. *ACS Nano* **2021**, *15* (3), 4608–4616. <https://doi.org/10.1021/acs.nano.0c08877>.
- (26) Dell, Z. E.; Schweizer, K. S. Theory of Localization and Activated Hopping of Nanoparticles in Cross-Linked Networks and Entangled Polymer Melts. *Macromolecules* **2014**, *47* (1), 405–414. <https://doi.org/10.1021/ma4021455>.
- (27) Poling-Skutvik, R.; Krishnamoorti, R.; Conrad, J. C. Size-Dependent Dynamics of Nanoparticles in Unentangled Polyelectrolyte Solutions. *ACS Macro Lett.* **2015**, *4* (10), 1169–1173. <https://doi.org/10.1021/acsmacrolett.5b00616>.
- (28) Smith, M.; Poling-Skutvik, R.; Slim, A. H.; Willson, R. C.; Conrad, J. C. Dynamics of Flexible Viruses in Polymer Solutions. *Macromolecules* **2021**, *54* (10), 4557–4563. <https://doi.org/10.1021/acs.macromol.1c00435>.
- (29) Poling-Skutvik, R.; Slim, A. H.; Narayanan, S.; Conrad, J. C.; Krishnamoorti, R. Soft Interactions Modify the Diffusive Dynamics of Polymer-Grafted Nanoparticles in Solutions of Free Polymer. *ACS Macro Lett.* **2019**, *8* (8), 917–922. <https://doi.org/10.1021/acsmacrolett.9b00294>.
- (30) Chen, Y.; Ma, R.; Qian, X.; Zhang, R.; Huang, X.; Xu, H.; Zhou, M.; Liu, J. Nanoparticle Mobility within Permanently Cross-Linked Polymer Networks. *Macromolecules* **2020**, *53* (11), 4172–4184. <https://doi.org/10.1021/acs.macromol.0c00334>.
- (31) Hall, D. B.; Deppe, D. D.; Hamilton, K. E.; Dhinojwala, A.; Torkelson, J. M. Probe Translational and Rotational Diffusion in Polymers near T_g : Roles of Probe Size, Shape, and Secondary Bonding in Deviations from Debye±Stokes±Einstein Scaling. **1998**.
- (32) Zhang, K.; Kumar, S. K. Molecular Simulations of Solute Transport in Polymer Melts. *ACS Macro Lett.* **2017**, *6* (8), 864–868. <https://doi.org/10.1021/acsmacrolett.7b00339>.
- (33) Zhang, K.; Meng, D.; Müller-Plathe, F.; Kumar, S. K. Coarse-Grained Molecular Dynamics Simulation of Activated Penetrant Transport in Glassy Polymers. *Soft Matter* **2018**, *14* (3), 440–447. <https://doi.org/10.1039/C7SM01941F>.
- (34) Xue, C.; Shi, X.; Tian, Y.; Zheng, X.; Hu, G. Diffusion of Nanoparticles with Activated Hopping in Crowded Polymer Solutions. *Nano Lett.* **2020**, *20* (5), 3895–3904. <https://doi.org/10.1021/acs.nanolett.0c01058>.

- (35) Mei, B.; Lin, T.-W.; Sheridan, G. S.; Evans, C. M.; Sing, C. E.; Schweizer, K. S. Structural Relaxation and Vitrification in Dense Cross-Linked Polymer Networks: Simulation, Theory, and Experiment. *Macromolecules* **2022**, *55* (10), 4159–4173. <https://doi.org/10.1021/acs.macromol.2c00277>.
- (36) Frenkel, D.; Smit, B. *Understanding Molecular Simulation: From Algorithms to Applications*; Academic Press: San Diego, CA, 2002.
- (37) Jain, T. S.; de Pablo, J. J. Influence of Confinement on the Vibrational Density of States and the Boson Peak in a Polymer Glass. *J. Chem. Phys.* **2004**, *120* (19), 9371–9375. <https://doi.org/10.1063/1.1689952>.
- (38) Riggelman, R. A.; Douglas, J. F.; de Pablo, J. J. Tuning Polymer Melt Fragility with Antiplasticizer Additives. *J. Chem. Phys.* **2007**, *126* (23), 234903. <https://doi.org/10.1063/1.2742382>.
- (39) Simmons, D. S.; Douglas, J. F. Nature and Interrelations of Fast Dynamic Properties in a Coarse-Grained Glass-Forming Polymer Melt. *Soft Matter* **2011**, *7* (22), 11010. <https://doi.org/10.1039/c1sm06189e>.
- (40) Mangalara, J. H.; Mackura, M. E.; Marvin, M. D.; Simmons, D. S. The Relationship between Dynamic and Pseudo-Thermodynamic Measures of the Glass Transition Temperature in Nanostructured Materials. *J. Chem. Phys.* **2017**, *146* (20), 203316. <https://doi.org/10.1063/1.4977520>.
- (41) Allen, M. P.; Tildesley, D. J. *Computer Simulation of Liquids, 2nd Ed.*; Oxford University Press: Oxford, 2017. <https://doi.org/10.1093/oso/9780198803195.001.0001>.
- (42) Kremer, K.; Grest, G. S. Dynamics of Entangled Linear Polymer Melts: A Molecular-Dynamics Simulation. *J Chem Phys* **1990**, *92* (8), 5057–5086. <https://doi.org/10.1063/1.458541>.
- (43) Rubinstein, M.; Colby, R. *Polymer Physics*; Oxford University Press, N. Y., 2003.
- (44) Tree, D. R.; Muralidhar, A.; Doyle, P. S.; Dorfman, K. D. Is DNA a Good Model Polymer? *Macromolecules* **2013**, *46* (20), 8369–8382. <https://doi.org/10.1021/ma401507f>.
- (45) Dutta, S.; Pan, T.; Sing, C. E. Bridging Simulation Length Scales of Bottlebrush Polymers Using a Wormlike Cylinder Model. *Macromolecules* **2019**, *52* (13), 4858–4874. <https://doi.org/10.1021/acs.macromol.9b00363>.
- (46) Coelho, J. F. J.; Carvalho, E. Y.; Marques, D. S.; Popov, A. V.; Percec, V.; Gil, M. H. Influence of the Isomeric Structures of Butyl Acrylate on Its Single-Electron Transfer-Degenerative Chain Transfer Living Radical Polymerization in Water Catalyzed by Na₂S₂O₄. *J. Polym. Sci. Part Polym. Chem.* **2008**, *46* (19), 6542–6551. <https://doi.org/10.1002/pola.22963>.
- (47) Minina, E. S.; Sánchez, P. A.; Likos, C. N.; Kantorovich, S. S. The Influence of the Magnetic Filler Concentration on the Properties of a Microgel Particle: Zero-Field Case. *J. Magn. Magn. Mater.* **2018**, *459*, 226–230. <https://doi.org/10.1016/j.jmmm.2017.10.107>.
- (48) Moreno, A. J.; Lo Verso, F. Computational Investigation of Microgels: Synthesis and Effect of the Microstructure on the Deswelling Behavior. *Soft Matter* **2018**, *14* (34), 7083–7096. <https://doi.org/10.1039/C8SM01407H>.
- (49) Plimpton, S. Fast Parallel Algorithms for Short-Range Molecular Dynamics. *J Comp Phys* **1995**, *117*, 1–19.
- (50) Nosé, S. A Unified Formulation of the Constant Temperature Molecular Dynamics Methods. *J. Chem. Phys.* **1984**, *81* (1), 511–519. <https://doi.org/10.1063/1.447334>.

- (51) Hoover, W. G. Canonical Dynamics: Equilibrium Phase-Space Distributions. *Phys. Rev. A* **1985**, *31* (3), 1695–1697. <https://doi.org/10.1103/PhysRevA.31.1695>.
- (52) Shavit, A.; Riggleman, R. A. Influence of Backbone Rigidity on Nanoscale Confinement Effects in Model Glass-Forming Polymers. *Macromolecules* **2013**, *46* (12), 5044–5052. <https://doi.org/10.1021/ma400210w>.
- (53) Bennemann, C.; Paul, W.; Baschnagel, J.; Binder, K. Investigating the Influence of Different Thermodynamic Paths on the Structural Relaxation in a Glass-Forming Polymer Melt. *J. Phys. Condens. Matter* **1999**, *11* (10), 2179–2192. <https://doi.org/10.1088/0953-8984/11/10/005>.
- (54) Riggleman, R. A.; Lee, H.-N.; Ediger, M. D.; de Pablo, J. J. Free Volume and Finite-Size Effects in a Polymer Glass under Stress. *Phys. Rev. Lett.* **2007**, *99* (21), 215501. <https://doi.org/10.1103/PhysRevLett.99.215501>.
- (55) Diaz Vela, D.; Simmons, D. S. The Microscopic Origins of Stretched Exponential Relaxation in Two Model Glass-Forming Liquids as Probed by Simulations in the Isoconfigurational Ensemble. *J. Chem. Phys.* **2020**, *153* (23), 234503. <https://doi.org/10.1063/5.0035609>.
- (56) Lin, E. Y.; Frischknecht, A. L.; Riggleman, R. A. Origin of Mechanical Enhancement in Polymer Nanoparticle (NP) Composites with Ultrahigh NP Loading. *Macromolecules* **2020**, *53* (8), 2976–2982. <https://doi.org/10.1021/acs.macromol.9b02733>.
- (57) McQuarrie, D. A. *Statistical Mechanics*; University Science Books: Sausalito, 2000.
- (58) Mei, B.; Schweizer, K. S. Activated Penetrant Dynamics in Glass Forming Liquids: Size Effects, Decoupling, Slaving, Collective Elasticity and Correlation with Matrix Compressibility. *Soft Matter* **2021**, *17* (9), 2624–2639. <https://doi.org/10.1039/D0SM02215B>.
- (59) Stillinger, F. H.; Hodgdon, J. A. Translation-Rotation Paradox for Diffusion in Fragile Glass-Forming Liquids. *Phys. Rev. E* **1994**, *50* (3), 2064–2068. <https://doi.org/10.1103/PhysRevE.50.2064>.
- (60) Hodgdon, J. A.; Stillinger, F. H. Stokes-Einstein Violation in Glass-Forming Liquids. *Phys. Rev. E* **1993**, *48* (1), 207–213. <https://doi.org/10.1103/PhysRevE.48.207>.
- (61) Kumar, P.; Buldyrev, S. V.; Becker, S. R.; Poole, P. H.; Starr, F. W.; Stanley, H. E. Relation between the Widom Line and the Breakdown of the Stokes–Einstein Relation in Supercooled Water. *Proc. Natl. Acad. Sci.* **2007**, *104* (23), 9575–9579. <https://doi.org/10.1073/pnas.0702608104>.
- (62) Becker, S. R.; Poole, P. H.; Starr, F. W. Fractional Stokes-Einstein and Debye-Stokes-Einstein Relations in a Network-Forming Liquid. *Phys. Rev. Lett.* **2006**, *97* (5), 055901. <https://doi.org/10.1103/PhysRevLett.97.055901>.
- (63) Kumar, S. K.; Szamel, G.; Douglas, J. F. Nature of the Breakdown in the Stokes-Einstein Relationship in a Hard Sphere Fluid. *J. Chem. Phys.* **2006**, *124* (21), 214501. <https://doi.org/10.1063/1.2192769>.
- (64) Mazza, M. G.; Giovambattista, N.; Stanley, H. E.; Starr, F. W. Connection of Translational and Rotational Dynamical Heterogeneities with the Breakdown of the Stokes-Einstein and Stokes-Einstein-Debye Relations in Water. *Phys. Rev. E* **2007**, *76* (3), 031203. <https://doi.org/10.1103/PhysRevE.76.031203>.
- (65) Ediger, M. D. Spatially Heterogeneous Dynamics in Supercooled Liquids. *Annu. Rev. Phys. Chem.* **2000**, *51* (1), 99–128. <https://doi.org/10.1146/annurev.physchem.51.1.99>.

- (66) Mei, B.; Lu, Y.; An, L.; Wang, Z.-G. Two-Step Relaxation and the Breakdown of the Stokes-Einstein Relation in Glass-Forming Liquids. *Phys. Rev. E* **2019**, *100* (5), 052607. <https://doi.org/10.1103/PhysRevE.100.052607>.
- (67) Mei, B.; Zhuang, B.; Lu, Y.; An, L.; Wang, Z.-G. Local-Average Free Volume Correlates with Dynamics in Glass Formers. *J. Phys. Chem. Lett.* **2022**, *13* (17), 3957–3964. <https://doi.org/10.1021/acs.jpcclett.2c00072>.
- (68) Berthier, L.; Biroli, G. Theoretical Perspective on the Glass Transition and Amorphous Materials. *Rev. Mod. Phys.* **2011**, *83* (2), 587–645. <https://doi.org/10.1103/RevModPhys.83.587>.
- (69) Mei, B.; Lin, T.-W.; Sing, C. E.; Schweizer, K. S. Glassy Dynamics and Mesh Confinement Effects on the Diffusive Motion of Molecular Penetrants. Pt. I: Theory. *Submitted*.
- (70) Zhang, R.; Schweizer, K. S. Correlated Matrix-Fluctuation-Mediated Activated Transport of Dilute Penetrants in Glass-Forming Liquids and Suspensions. *J. Chem. Phys.* **2017**, *146* (19), 194906. <https://doi.org/10.1063/1.4983224>.

Supporting Information Figures

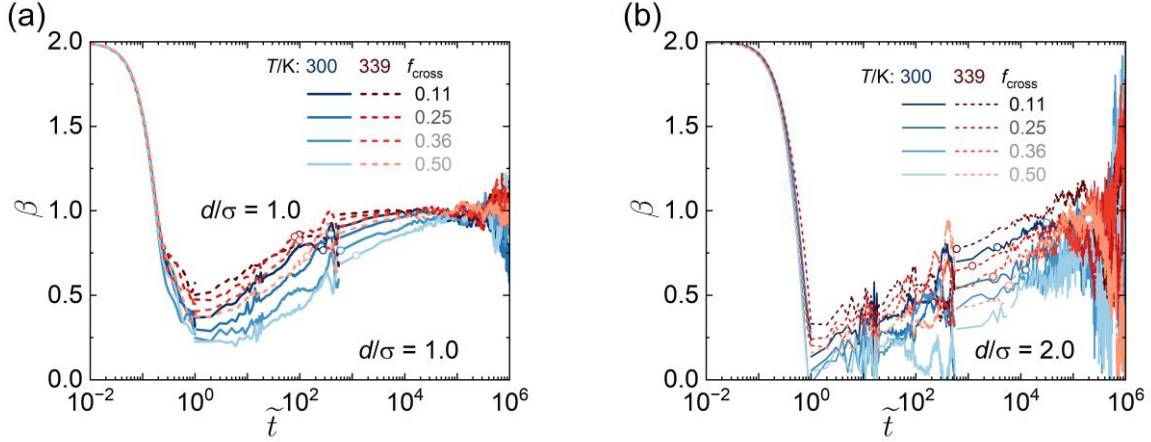


Figure S1. Representative plots of the effective exponent β for the mean square displacement versus time $\langle \tilde{r}_p^2(\tilde{t}) \rangle \sim \tilde{t}^\beta$ of a penetrant particle with sizes (a) $d/\sigma = 1.0$ and (b) $d/\sigma = 2.0$, for the same values of T and f_{cross} as shown in **Figure 2**. β is the slope of **Figure 2**, and both plots show that penetrant diffusion reaches the Fickian diffusion limit of $\beta = 1$ in the long-time region. The open circles denote the length scale of the polymer network mesh size, as described in **Table S1**. Intermediate regions with more noise reflect the need to perform several distinct computational runs with different data output frequency.

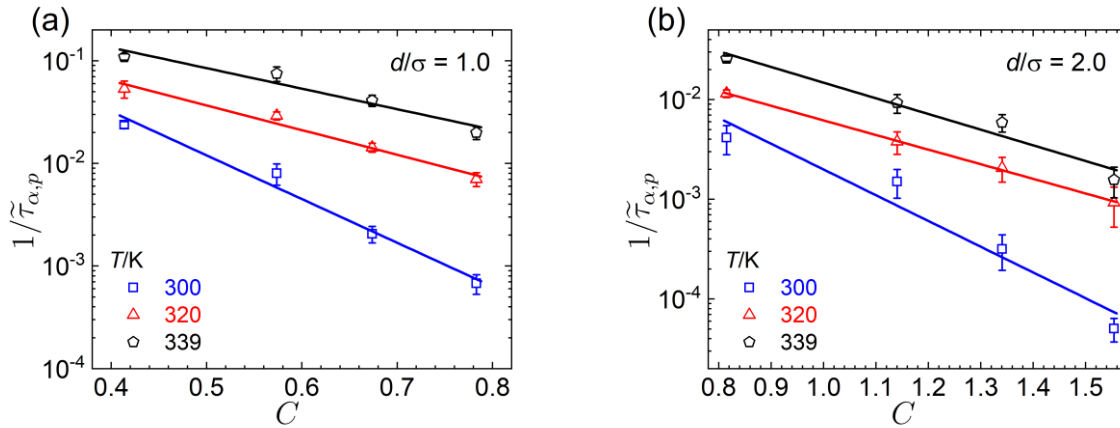


Figure S2. The inverse penetrant alpha time $1/\tilde{\tau}_{\alpha,p}$ plotted with respect to the confinement ratio C for penetrant particles with sizes (a) $d/\sigma = 1.0$ and (b) $d/\sigma = 2.0$. For both particle sizes, we find that they are consistent with the trend $\tilde{\tau}_{\alpha,p} \propto \exp(-bC)$. This primarily reflects the local glassy dynamics and *not* mesh confinement effects, and so this trend contributes to the apparent degeneracy between the two mechanisms for crosslink effects on penetrant transport in networks.

Figure S3:

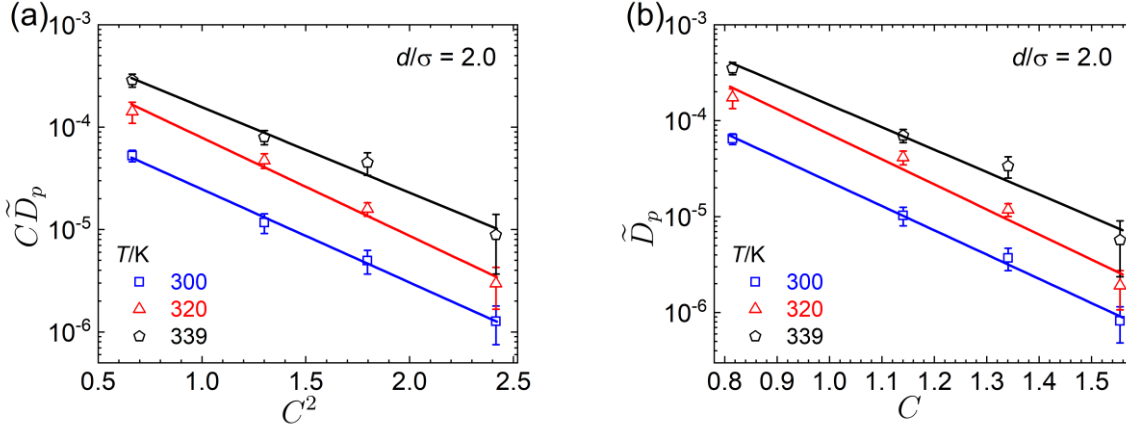


Figure S3. The penetrant diffusion constant \tilde{D}_p plotted with respect to the confinement ratio C as suggested by the forms of various literature predictions for mesh confinement effects. (a) Cai, *et al.*²³ predicts that $\tilde{D}_p \propto C^{-1} \exp(-C^2)$ and (b) Dell and Schweizer²⁶ predict that $\tilde{D}_p \propto \exp(-bC)$. Both ways of plotting this data appear linear, even though mesh confinement does not play the sole role in penetrant transport for the $d/\sigma = 2.0$ case plotted here.

Table S1. Mesh size (in unit of σ) of networks at various f_{cross} .

f_{cross}	0.11	0.25	0.36	0.50
$d/\sigma = 1.0$	2.43	1.75	1.48	1.28
$d/\sigma = 2.0$	2.45	1.76	1.49	1.29